THESIS FOR THE DEGREE OF LICENTIATE OF ENGINEERING

Increased Productivity of Ferrous Alloys Produced by Powder Bed Fusion – Laser Beam

RASMUS GUNNEREK

Department of Industrial and Materials Science

CHALMERS UNIVERSITY OF TECHNOLOGY

Gothenburg, Sweden 2024

Increased Productivity of Ferrous Alloys Produced by Powder Bed Fusion – Laser Beam
RASMUS GUNNEREK

Technical report no IMS-2024-3

Department of Industrial and Materials Science
Chalmers University of Technology
SE-412 96 Gothenburg
Sweden
Telephone + 46 (0)31-772 1000

Chalmers digitaltryck
Gothenburg, Sweden 2024

Abstract

Low production speeds limit wider adoption of powder bed fusion – laser beam (PBF-LB) in cost sensitive industries as it correlates directly with high production costs. The main process parameters such as scan speed, hatch distance and layer thickness can be scaled up to increase build speed, but it often comes at a trade off in lower quality, i.e. surface roughness, porosity/density and mechanical properties. The objective of this thesis study was to investigate how large build rates influences microstructure and processability of two low alloy steels (4130 and 4140) and 316L stainless steel by detailed characterization of defects and porosity present in relation to process parameters applied.

The initial study found that achieving consistent processability of low alloy steels across layer thicknesses, as indicated by the as-printed density, is better correlated with surface energy density (SED) J/mm^2 rather than volumetric energy density (VED) J/mm^3. Regions with high densities above 99.8% exhibited similar ranges of SED at different layer thicknesses, explained by the resulting melt pool depths being more similar than at similar ranges of VED.

The second study addressed the impact of three- and four-factor increase in hatch distance and layer thickness compared with state of the art. It was observed that the influence of VED on density was poorly described as differences of up to 7.5% in density were measured at the same VED. More accurate representations of impact on main print parameters on density was found by regression analysis which also captured the interaction between laser power, scan speed and hatch distance at different layer thicknesses. Build rate increase can be realized by numerous combinations of basic laser parameters, however this results in distinctive porosity characteristics and even at the same levels of build rate increase, pore characteristics, such as orientation, aspect ratio and size, can differ significantly.

Keywords: additive manufacturing, powder bed fusion – laser beam, 316L stainless steel, low alloy steel, porosity, build speed, build rate, productivity in AM, process optimization.

Preface

This licentiate thesis presents work conducted at the Department of Industrial and Materials Science at Chalmers University of Technology from September 2020 to March 2024. The studies have been performed within the frame Centre for Additive Manufacturing – Metal (CAM^2), supported by the Swedish Governmental Agency of Innovation Systems (Vinnova). The work was supervised by Professor Eduard Hryha and Dr. Zhuoer Chen (during 2020 and 2021) and Professor Lars Nyborg as examiner.

List of appended papers

Paper I: **Improving productivity of low-alloy steels produced by powder bed fusion – laser beam**

Rasmus Gunnerek, William Hearn, Eduard Hryha

Manuscript

Paper II: **Impact of high-productivity process parameters in powder bed fusion – laser beam on microstructure of stainless steel 316L**

Rasmus Gunnerek, Zhouer Chen, Eduard Hryha

European Journal of Materials, 2023, DOI: https://doi.org/10.1080/26889277.2023.2292987

Contribution to appended papers

Paper I: The author planned and performed a major part of the experimental work and analysed the results. The author wrote the paper with co-authors.

Paper II: The author planned and performed a major part of the experimental work and analysed the results. The author wrote the paper with co-authors.

Table of Contents

1. Introduction

1.1 Background

Powder bed fusion – laser beam (PBF-LB) is considered as one of the most prominent additive manufacturing processes. The PBF-LB utilizes a high energy laser source to consolidate metal powder in a layer-by-layer manner directly from computer aided designs (CAD) files to achieve desired 3D structures [1–3]. Some benefits include reduction in material waste, high part complexity and reduced lead times compared to conventional manufacturing technologies. However, to reach broader industrialization of the process costs need to be reduced. The high costs come from different aspects in the PBF-LB process chain. Ensuring high quality sets high demand on powder characteristics and process parameters to prevent process instabilities.

Productivity has been approached in several aspects. Multiple laser systems shorten the build time required to expose and consolidate each layer but also introduce new complexity to the process such as laser interaction [4]. Build time can also be reduced by increasing the build rate, which is governed by process parameters mainly: laser power, scan speed, layer thickness and hatch distance. A combination of great layer thickness, hatch distance, laser power and scan speed are typically used to lower build time, but it often comes at the cost of lower density. Consequently, increased productivity can significantly impact the material and mechanical properties of PBF-LB components.

Structural steels as e.g. low alloy steels are found in cost sensitive industries that could benefit from the on-demand printing and shortened lead times offered by PBF-LB, especially in after-market sector. Significant part of the cost in PBF-LB manufacturing chain is related to the long print times. By scaling up main printing parameters, the costs could significantly be reduced. This would possibly come as a trade-off with larger fraction of defects in PBF-LB components. However, many cast and powder metallurgy components in automotive can tolerate porosity levels up to 5 %. The issue lies in the understanding the impact of porosity fraction and its characteristic on mechanical properties, assure necessary process robustness and further design components for respective microstructure and properties. Hence, this thesis adds to the understanding of how defects such as porosity are connected to the processing parameters in case of high productivity PBF-LB processes for the low alloy steels and 316L stainless steel. Emphasis was to capture how different process parameters correlate to pore fraction and characteristics, in particular size, morphology, distribution, and orientation, as it will influence mechanical properties.

1.2 Research objectives

The intended objective of this research can be formulated by the following two research questions:

1) What is the impact of PBF-LB process parameters on build speed during processing of iron-based alloys?

2) What is the impact of increased build speed during PBF-LB processing on porosity characteristics and material properties?

2. Powder bed fusion – laser beam

2.1 Principle of Powder bed fusion – laser beam

Powder bed fusion – laser beam (PBF- LB) uses a high energy laser source to selectively melt powder in a powder bed based on a CAD – file in a layer-by-layer fashion creating 3D structures. This enables high complexity and geometrical freedom in comparison to conventional manufacturing methods. With the current knowledge of the process, structural components of high density and good mechanical properties can be built in a variety of metal alloys suited for different applications as e.g., stainless and tool steels [5], nickel-based super alloys [6], aluminium alloys [7] ,titanium alloys [8], etc. The ability to manufacture components with necessary performance on demand with reduced lead times and high material utilization have attracted many industries such as the aerospace, automotive and medical industry [9].

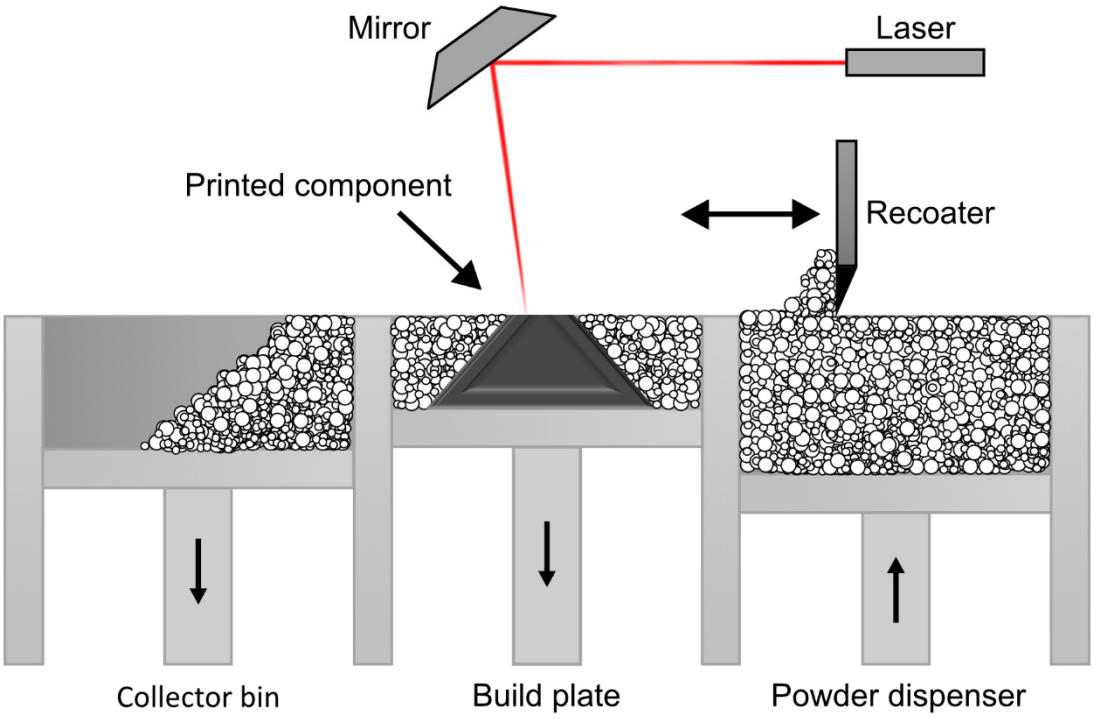

Figure 1. Illustration of the working principle of PBF-LB and its main components.

Figure 1 illustrates the main principle of PBF-LB where the powder dispenser is loaded with metal powder that is dispersed in a thin layer on to the build plate by a recoater blade. Based on the pre-defined geometry, mirrors navigate the laser source providing localized melting and solidification. After each layer is completed, the build plate is lowered, and a new layer is applied. This procedure is repeated until the defined 3D structure is achieved [2]. Excessive powder from the collector bin and powder surrounding the built component can be used in subsequent builds offering high material utilization. To prevent impurities and oxidation the

PBF-LB is performed in an inert environment using gases such argon, nitrogen or helium [10]. A constant gas flow during the build also prevents ejected powder particles from contaminating the powder bed or solidified regions of the component.

2.2 Process parameters in Powder Bed Fusion – Laser Beam

There are approximately 100 process related parameters which affect the outcome of a print [11,12]. However, this thesis study is narrowed down to the main process parameters that are directly identified as responsible for the quality of a build i.e., laser power (*p*), scan speed (*v*), layer thickness (*t*) and hatch distance (*h*). The connection between the main printing parameters and the generated melt pool dimensions is illustrated in Figure 2.

The laser power governs the size of the melt pool depth (*D*) and width (*W*) and thus the local temperature gradient experienced by the powder bed. Laser power ranges from 50 to 1000 W depending on the machine system and is dependent on the material melting temperature, powder size etc [2]. It is important to use adequate laser power to provide complete fusion and bonding with previous layers and neighboring melt tracks, but excessive laser power can lead to evaporation and instabilities of the melt pool. The velocity in which the laser beam scans the surface is called the scan speed. The scan speed controls, in combination with laser power and layer thickness, the melt pool geometry of a melt track. High scan speeds lead to shallow and narrow melt pools, characterized by high solidification rates whereas lowering the speed yields deeper and wider melt pools and thus slower solidification rates. Layer thickness is the predefined distance which the build plate is lowered before each deposit of new powder. Typically, 20 to 100 µm layer thicknesses are used depending on the requirements on the final component. Fine layers yield higher geometrical accuracy and less rough surfaces. Adequate layer thickness is necessary to provide proper bonding with previous layers. Therefore, it is important that the melt pool depth is larger than the layer thickness. To prevent unmelted powder between neighboring scan tracks, a sufficient overlap is required which is decided by the hatch distance [13,14]. The hatch distance needed is dependent on the spot size of the laser and the melt pool depth/width yielded based on scan speed and laser power in a specific layer [13]. Proper overlap is also influenced by the layer thickness and the scan rotation as remelting of a certain volume of material increases with finer layer thickness which can compensate for defects generated in previous layers.

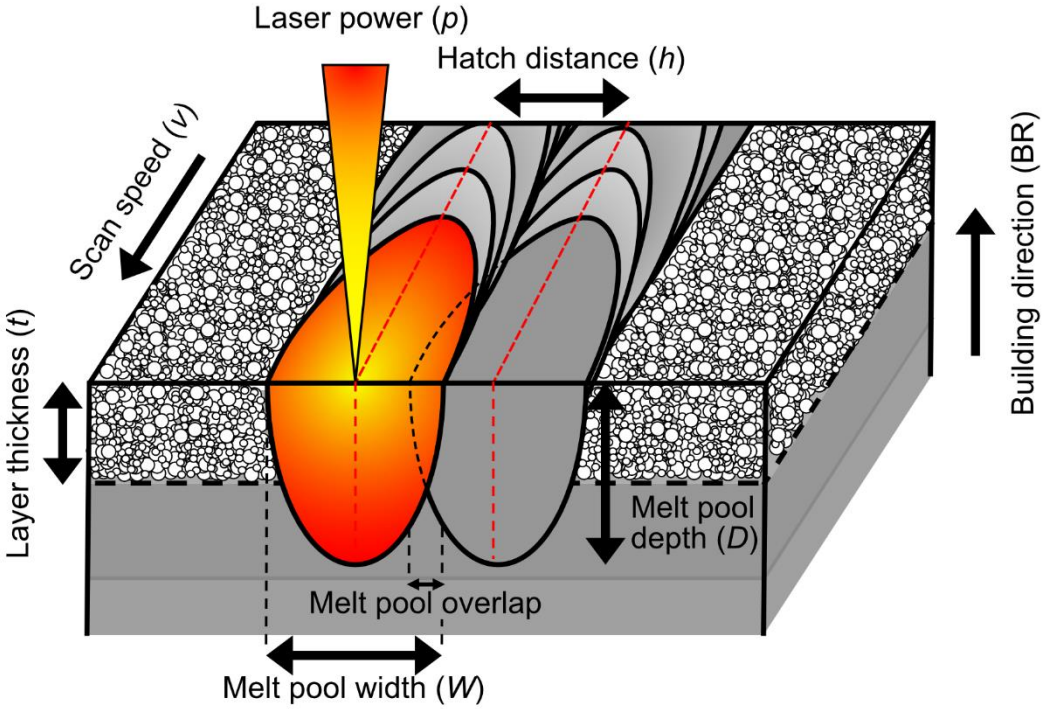

Figure 2. The connection between main printing parameters and the resulting melt pool characteristics.

To give a simplistic view of the connection between printing parameters and their performance, the main printing parameters are combined and evaluated based on e.g., obtained density, microstructure and mechanical properties [3,15]. The volumetric energy density (VED), measured in J/mm^3 (eq. 1) is the energy imparted per unit volume and is utilized to indicate optimum ranges of laser power, scan speed, hatch distance and layer thickness towards some wanted criteria. However, there are limitations of the VED as it does not explain the complex phenomena which drives mass and heat transfer inside the melt pool [16]. Therefore, VED should be used only as an indication of processability.

$$VED = \frac{p}{v \cdot h \cdot t} \left(\frac{J}{mm^3}\right) \quad (1)$$

By removing layer thickness from VED, the surface energy density (SED), measured in J/mm^2 is obtained, see eq. 2. The SED has shown to yield decent correlation with the melt pool depth and melt pool width [17,18]. Whereas others used SED to evaluate the overlap between neighboring melt pools within a single layer [12], process windows have also been shown to correlate well with SED in terms of obtained hardness, density, microstructure and phases present [19].

$$SED = \frac{p}{v \cdot h} \left(\frac{J}{mm^2}\right) \quad (2)$$

An even more simplified combined parameter is the linear energy density (LED), measured in J/mm (eq. 3), solely a function of laser power and scan speed which describes the energy input per unit length, which is commonly used to validate stability and morphology of single-track experiments [20].

$$LED = \frac{p}{v} \left(\frac{J}{mm}\right) \quad (3)$$

2.3 Defects in Powder Bed Fusion – Laser Beam processed components

2.3.1 Porosity

Defects can form at different stages of the process where porosity is one of the more common types. Porosity can be categorized into process induced pores or powder feedstock pores. In this context, process induced porosity will be referred to those which are generated by the interaction between printing parameters, namely laser power, scan speed, hatch distance and layer thickness. The connection between the combination of parameters and type of porosity is a result of the melt pool and the melt track geometry that is generated, see Figure 2. During PBF-LB it is desirable to use such process parameters that generate a stable semi spherical melt pool geometry which is achieved by operating in conduction mode [21]. If the parameters are combined in such case that the melt pool becomes more elongated and deviates from the stable semi spherical morphology, it enters the keyhole melting mode. This section covers the complex relationship between process parameters, the melt pool they generate and how these interactions induce different types of porosity.

Gas porosity

The powder feedstock in PBF-LB is commonly produced by gas atomization. During gas atomization, high pressure inert gas is sprayed towards a molten metal flow which breaks it into droplets that spheroidizes upon contact with the surrounding media. In this rapid sequence, small pores (<10 µm) can become entrapped inside the metal powder and are thereby called gas porosity [22,23]. Although, most of the gas porosity is removed during PBF-LB process, some can remain in the microstructure. The relatively small size and spherical shape is not considered detrimental for mechanical properties [22,24].

Lack of fusion

Lack of fusion porosity is generated if the energy provided by the process is insufficient to provide cohesion between layers or neighbouring melt tracks, see Figure 3. Lack of fusion between layers occur when melt pools are shallow and lack enough penetration for proper bonding with previously built layers which leave large, elongated pores stretching perpendicular to the build direction (Figure 3a) [3]. The lack of proper overlap between subsequent melt tracks also forms lack of fusion. However, the orientation of such pores is more aligned parallel with the build direction and could be connected through several layers (Figure 3b) [3,25]. Compared to other types of pores, lack of fusion porosity is characterized by sharp and irregular shape which can act as stress concentrations for crack initiation during mechanical loading and thus reduce the mechanical performance of PBF-LB components. It is therefore recommended to tailor the process to keep lack of fusion porosity to a minimum.

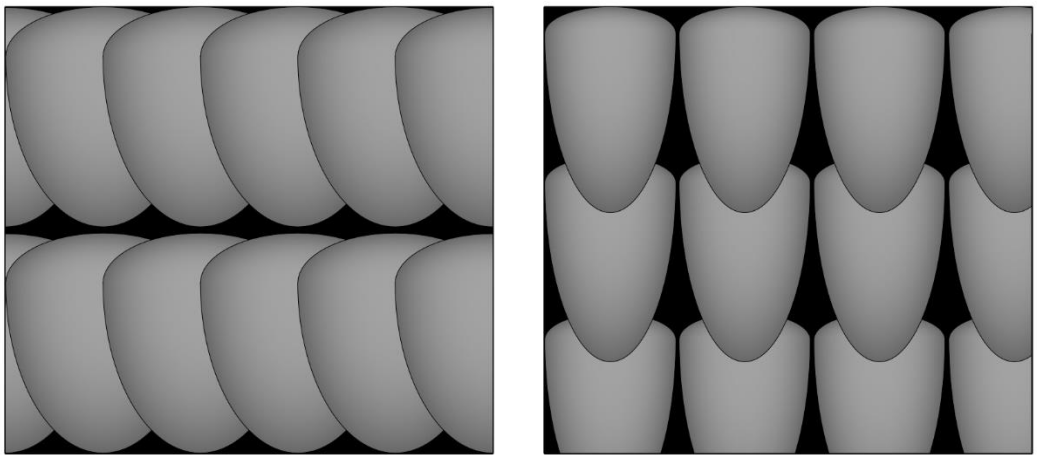

Figure 3. Simplistic view of porosity resulting from a) lack of fusion between layers and b) insufficient overlap between neighbouring melt pools.

Keyhole porosity

Large energy input generated by e.g. low scan speed and high laser power can lead to a transition from stable conduction mode into keyhole mode. Melt pools generated in keyhole mode are generally deep and narrow leading to large local thermal gradients. During such conditions evaporated metal develops and exerts large recoil pressure with forces acting towards the bottom of the melt pool [24]. The combination of recoil pressure and narrow waists can lead to vaporized metal at the bottom not having sufficient time to escape and leave pores of semi spherical appearance in the microstructure [21,22,24,25]. The highly dynamic flow inside the melt pool and movement of the keyhole during short time intervals are depicted in Figure 4. The clockwise motion of melt behind, and the impact of upward/downward motion in

front of the keyhole, creates bulges along the keyhole which results in necking (Figure 4a-b). The loss in keyhole diameter due to necking results in less energy supplied and the bottom of the keyhole freezes as it gets caught by the liquid/solid interface (Figure 4b). When the keyhole reaches the solid interface a keyhole pore is retained in the microstructure (Figure 4c). Keyhole pores can be mitigated by decreasing the laser power or increasing the scan speed which reduces the energy input. However, due to the spherical shape keyhole pores are less harmful for mechanical properties compared to lack of fusion pores [26].

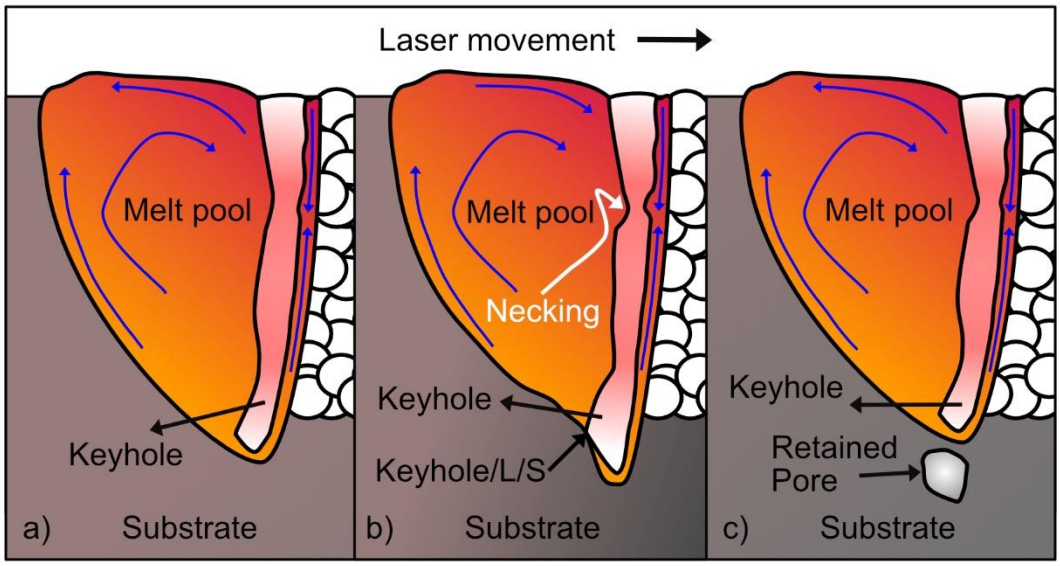

Figure 4. a) - c) Simplified sequence of mechanism behind keyhole pore formation and the complex movement inside the melt pool inspired by [21].

Spatter

The highly dynamic process conditions within and in the vicinity of the melt pool can lead to ejection of metal droplets or powder across the powder bed called spatter. There are different types of spatters which can roughly be divided into cold and hot spatter due to the formation mechanism [27]. Hot spatter is generated due recoil pressure which causes instability in the melt pool whereas cold spatter is more driven by the interaction and entrainment with the process gas [27,28]. These spatter particles can influence the quality during the printing process in different aspects. Consequently, spatter could induce large lack of fusion pores in the microstructure.

2.3.2 Cracks

Due to the large solidification rates (10^3-10^8 $^\circ C \cdot s^{-1}$) [29] great residual stresses develop in PBF-LB that depending on material processed can lead to cracking [30]. Cold cracking is a type of

crack commonly found in high carbon containing steels as it promotes formation of brittle and hard martensite phase during cooling. In conventional welding processes, an increase in hardenability by high carbon equivalent correlates well to increased risk of cold cracking [31]. To mitigate cold cracking several aspects have been touched to lower the residual stresses. Operating at larger VED provides increased cyclic reheating due to larger melt pool dimensions which yields lower thermal gradients and thus lower risk of cold cracking [32]. Further, most PBF-LB systems offer build plate preheating which can help to prevent cold cracking by lowering thermal gradients and cooling rates during the process [33].

2.4 Powder Bed Fusion – Laser Beam of ferrous alloys

2.4.1 316L stainless steel

The stainless steel 316L is one of the most studied alloys in PBF-LB due to its excellent processability [34]. The 316L contains high contents of chromium and nickel which stabilizes the austenitic gamma phase at room temperature and thus prevents formation of brittle martensite. Due to its one phase material, it is not a coincident that it is one of the more heavily studied alloys for PBF-LB. The alloy is attractive for its combination of strength and elongation while exhibiting excellent corrosion properties. It is thereby commonly used in energy, food, medical and pharmaceutical applications. The large local temperature gradients, following the fine local melting and cooling, yield a complex network of non-equilibrium features. It consists of columnar grains and overlapping melt pools oriented in the build direction built up by fine cellular structures which result in properties comparable with or even better than conventionally produced 316L materials [35]. Grain boundaries and cell walls hinder dislocation movement. The cell walls are rich in solute atoms such as molybdenum and chromium, which in corporation with the high dislocation density result in high strength [15,36,37].

2.4.2 Low alloy steel

Low alloy steels are ferrous alloys containing less than 8 wt.% alloying elements. The low alloying additions of elements e.g. Cr, Mo, Mn improves hardenability and strength compared to plain carbon steels at moderate costs. The maturity of low alloy steels has not reached the same level in PBF-LB as single phase materials such as 316L due to the phase transformation to martensite that in case of higher carbon contents promotes cracking due to martensite brittleness, especially at high residual stresses. Therefore, studies of PBF-LB produced low alloy steels have been limited so far to defect mitigation and to develop process strategies to enhance the processability. Some of the studied low alloy steels are AISI 4130 [33,38–42], AISI 4140 [17,31,33,39,43] and AISI 4340 [33,39,44,45].

2.5 Productivity of ferrous alloys

Increasing productivity is important as low alloy steels are most used in industries reliant on serial production (e.g., automotive) and are sought after due to their good structural performance at relatively affordable costs [46]. This is unlike more traditionally produced PBF-LB components that are used for niche production where small production volumes and complex geometries are required, with lower sensitivity to high production costs [47]. One potential segment that could benefit from the process and material is in production of spare parts. Spare parts are usually bought and put on shelves which includes both, locked up uncertain capital and requires high storage and inventory costs, especially considering that up to 80% of spare parts are never used [48]. Here, the flexibility and on demand benefits of PBF-LB could lower costs, save up storage and be more sustainable [49]. Therefore, for these materials to be adopted in the relevant industries, improvements in productivity and processability during PBF-LB are necessary to increase robustness and cut down manufacturing costs.

The productivity of the PBF-LB process is to a large extent influenced by the choice of the process parameters such as the laser power, scan speed, hatch distance and layer thickness. Small layer thicknesses (20-40 µm) are typically used to ensure adequate quality of prints i.e., low porosity, smooth surfaces, and dimensional accuracy. Among the four main process parameters, the layer thickness is identified as the one parameter directly responsible for influencing productivity [35,50]. Studies on increased layer thicknesses for one phase metals such as 316L stainless steel show that in general material properties are kept on the level determined by the material standards, even though some properties as e.g., ductility, is reduced [35,51]. As low alloy steels have added complexity due to the martensitic transformation, material sensitivity when it comes to processability at larger layer thicknesses is also expected to increase.

Commonly defined by the volume of material built per time unit (cm^3/h), the build rate refers to the sequence during the process when the laser is scanning across the surface (eq 4). Meanwhile, the idle time is the time required to deposit new powder in between subsequent runs. As an increased layer thickness decreases the total number of layers required to build a certain volume of material, it also reduces the overall build time. Therefore, there is a motivation to push the layer thickness to increase productivity and lower costs of PBF-LB components.

$$\text{Build rate} = v \cdot h \cdot t \left(\frac{cm^3}{h}\right) \quad (4)$$

By taking developed parameters for 316L metal powder as state-of-the-art on the same machine system used in this licenciate thesis, provided by EOS M290 (EOS GmBh, Germany), current build rates possible, while achieving densities of ~99.9 at 40 µm layer thickness and ~99.8 at 80 µm layer thickness, maximizes at approximately 13 cm^3/h and 30 cm^3/h, respectively [52]. Notice that by increasing the layer thickness by factor of two the build rate is also doubled.

3. Materials and experimental setup

3.1 Materials and PBF-LB system

In this thesis study samples were produced on an EOS M290 (EOS GmbH, Germany) PBF-LB machine using 316L stainless steel and AISI 4130 and 4140 low alloy steel powders provided by Höganäs AB. The 316L powder had a powder particle size distribution of 20 – 53 µm. The powder size distribution for the low alloy steels were measured by a Mastersizer 3000, see table 1. Nominal composition of each powder is presented in table 2.

Table 1. Powder particle size distribution of low alloys steels

	D_{10} (µm)	D_{50} (µm)	D_{90} (µm)
AISI 4130	28.7	43.5	64.8
AISI 4140	25.9	39.8	60.2

Table 2. Chemical composition (wt. %) of studied ferrous alloys

	C	Cr	Mo	Ni	Mn	Si	O	Fe
AISI 4130	0.34	1.0	0.20	-	0.60	0.30	0.05	Balance
AISI 4140	0.47	1.0	0.20	-	0.60	0.20	0.07	Balance
AISI 316L	0.028	16.9	2.5	12.6	1.5	0.7	0.056	Balance

3.2 Design of experiment strategies for increased build rates

There are multiple strategies used in process development connected to parameter optimisation. In PBF-LB, a common approach is to combine the main process parameters into the VED, which is a combined parameter of laser power (W), scan speed (mm/s), hatch distance (mm) and layer thickness (mm). The VED (J/mm^3) is thus a simplistic function to evaluate how combinations of these parameters correlate to the obtained density, microstructure and mechanical properties. However, VED has its limitations as the same VED can be reached through multiple combinations of the parameters. Especially, the melt pool characteristics can be significantly different at the same VED [16]. Therefore, it is recommended that only few parameters are varied when using VED as a design parameter.

To achieve the same VED at a 2 factor increase in layer thickness, significant reductions in hatch distance or scan speed are required. Consequently, different melt pool characteristics are obtained at different layer thicknesses. In paper 1, that studies the influence of layer thickness on build rate, another function was introduced referred to as SED, measured in J/mm^2 which removes the layer thickness from the VED equation. Assumption is that melt pool

characteristics would be more similar at the same SED for different layer thicknesses. A summary of these parameters is found in table 3. Here, the hatch distance was kept at a constant 70 µm and the SED was varied by the scan speed at 3 settings of laser power based on parameter development at 20 µm layer thickness [53].

Table 3. Investigated parameters in paper 1 based on SED and VED varied by altering scan speed and laser power

Laser power (W)	170	210	250
Scan speed (mm/s)	640–1012	790–1250	940–1490
SED (J/mm^2)	2.4–3.8	2.4–3.8	2.4–3.8
VED (J/mm^3) 40 µm	60–95	60–95	60–95
VED (J/mm^3) 60 µm	40–63	40–63	40–63

In paper 2, more dedicated design of experiments was developed, where build rate increases by scan speed, hatch distance and laser power were studied across a wide process region and four different layer thicknesses, see table 4. To limit the number of samples to predict the influence of main parameters on density (%), through linear regression (see eq. 5), a combination of linear constraints and the modern I-optimal design was utilized. Linear constraints were constructed based on previous knowledge of VED [35]. The I-optimal design space (see Figure 5) consists of 24 data points at each layer thickness.

$$Density = (100 - Porosity) = \big(100 - f(p, v, h)\big) = p + v + h + p^2 + p \cdot v + v^2 + p \cdot h + v \cdot h + h^2 \quad (5)$$

Table 4. Parameters studied in paper 2 at 20, 40, 60 and 80 µm layer thickness

Parameter	lower	upper
Laser power (W)	195	280
Scan speed (mm/s)	600	1800
Hatch distance (µm)	90	270

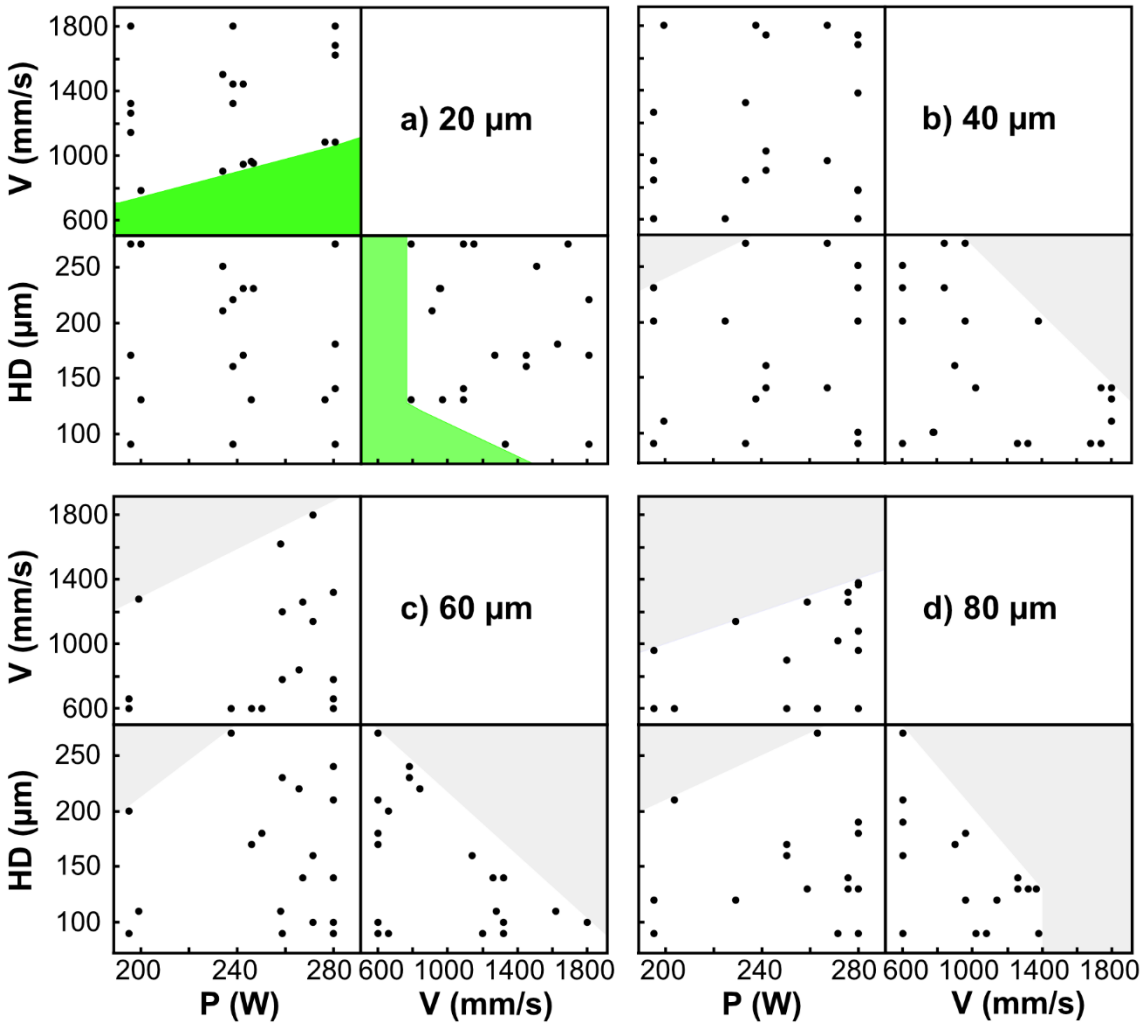

Figure 5. Graphical representation of the design space separated by layer thickness (20 -80 µm). The upper (green) and lower (grey) constraints for VED restrict the design space.

3.3 Characterization

3.3.1 Metallography

In preparation for microstructural characterization, samples manufactured were removed from the build plate using electric discharge machining (EDM). Each sample was then carefully sectioned along the BD-X plane using a Buehler Isomet 2000 precision saw and then mounted in Polyfast resin. Subsequently, the samples were subjected to grinding using SiC foil on a Struers TegraPol with grit sizes ranging from 320 to 2000. Fine polishing was conducted,

employing 3 µm and 1 µm diamond suspension to obtain a mirror-finish. Samples in the as-polished state were used for density measurements and pore characteristics but also to perform hardness tests in Paper 1.

To reveal the microstructure and more specifically melt pool boundaries, 3% Nitral solution was used for the martensitic low alloy steels, while the austenitic 316L underwent electrochemical etching in 10% oxalic acid with a constant potential of 3V and a platinum cathode. The melt pool width (µm) and depth (µm) were estimated and averaged across 30 melt pools at the top surface of each sample in both studies.

3.3.2 Light optical microscopy (LOM)

Micrographs of as polished and etched samples were captured by means of light optical micrography (LOM) on a Zeiss Axiovision 7 at × 5 magnification (0.88 µm × 0.88 µm per pixel). The microscope was set by the proprietary software to take images in sequence to yield a large area. These images were montaged to form a large micrograph covering a sampled 5 × 5 mm^2 area. The images were saved in 8-bit grayscale format (grey value ranging from zero to 255) and evaluated using the Matlab image processing toolbox and the porosity level was calculated on binary images using a 170 threshold in grey value in paper 2. Stitched micrographs were cropped to separate the bulk material from the mount resin in each image. Shape descriptors of interest, namely orientation, major axis length, minor axis length and aspect ratio of each pore, were calculated by the *regionprops* feature in Matlab. It can be seen how the shape descriptors are correlated in relation to sample cross sections in Figure 6. In paper 1 the ImageJ software by Fiji was utilized in the work performed on low alloy steel following the guidelines in [54].

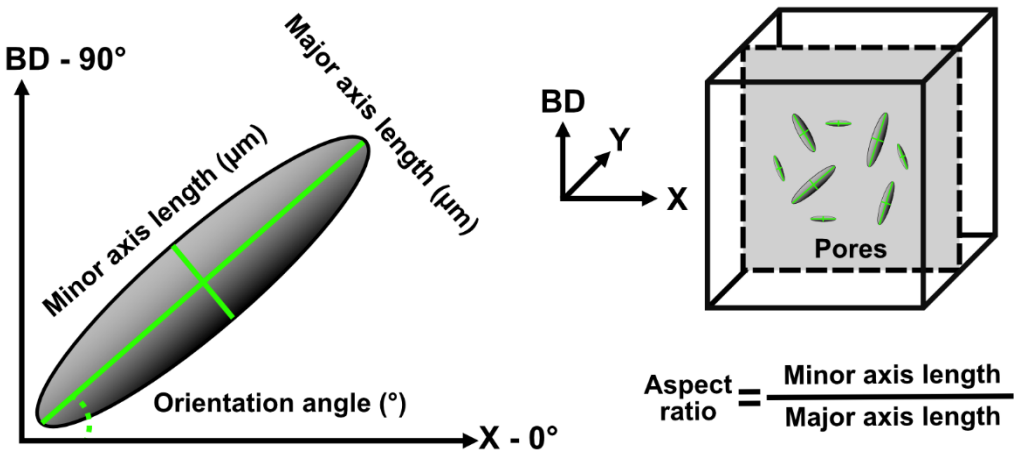

Figure 6. Pore characteristics of interest in paper 2.

3.3.3 Hardness testing

In paper 1, a DuraScan 70-G5 was used to perform 16 Vickers hardness (HV10) microhardness indentations in a 4 x 4 grid distanced 2.5 mm apart on each sample to evaluate the influence of process parameters on the hardness. This was done in accordance with ASTM – standards E384 – 17 [55].

4. Summary of appended papers

In this chapter the results from attached manuscripts are summarized and discussed in relation to the research questions.

Both research questions are investigated in paper 1 and 2. Paper 1 addressed the impact of layer thickness on build speed of two low alloy steels of different carbon content by characterizing defects present. Paper 2 included a more detailed description of the effect of main process parameters on pore characteristics at increased build rates of 316L stainless steel.

4.1 Summary of results Paper 1 – Impact of layer thickness on low alloy steels

The motivation of paper 1 was to investigate the ability to boost build speed of low alloy steels produced by PBF-LB using the parameter development, presented in [53] as a baseline. Low alloy steels are commonly found in cost sensitive sectors such as in the automotive industry [56]. To lower costs of the process and thus the feasibility of using this technology, the study focused on the impact of increased layer thickness which is identified as the most influential parameter to lower build time [35,57].

Influence of layer thickness on density

Figure 7 shows impact of SED of between 2.4 and 3.8 J/mm^2 on density evolution of Figure 7 a) – b) the 4130 and Figure 7 c) – d) the 4140 alloy at separate layer thicknesses. Both alloys showed similar trends of enhanced densification with larger SED. At the 40 µm layer thickness densities of 99.7 % (4140) and 99.5 % (4130) was measured at 2.4 J/mm^2 and reached peak values of 99.9 % as the SED increased, see Figure a) and Figure c). Consequently, a wide printing region is observed at 40 µm layer thickness and there is no noticeable impact of the laser power used. However, at 60 µm layer thickness a clearer impact of the laser power and SED is seen. For both alloys higher density is measured by using larger laser power (<3.2 J/mm^2). Past this value densities above 99.8 % are reached for 210 and 250 W laser power. It is important to note that the 170 W laser power fails to reach density values above 99.5 %. Here, a reduction in density is seen by further increases above 3.4 J/mm^2. Thus, an increased layer thickness reduces the SED range in which densities above 99.8 % are obtained. Also, the importance of using higher laser power increases with layer thickness.

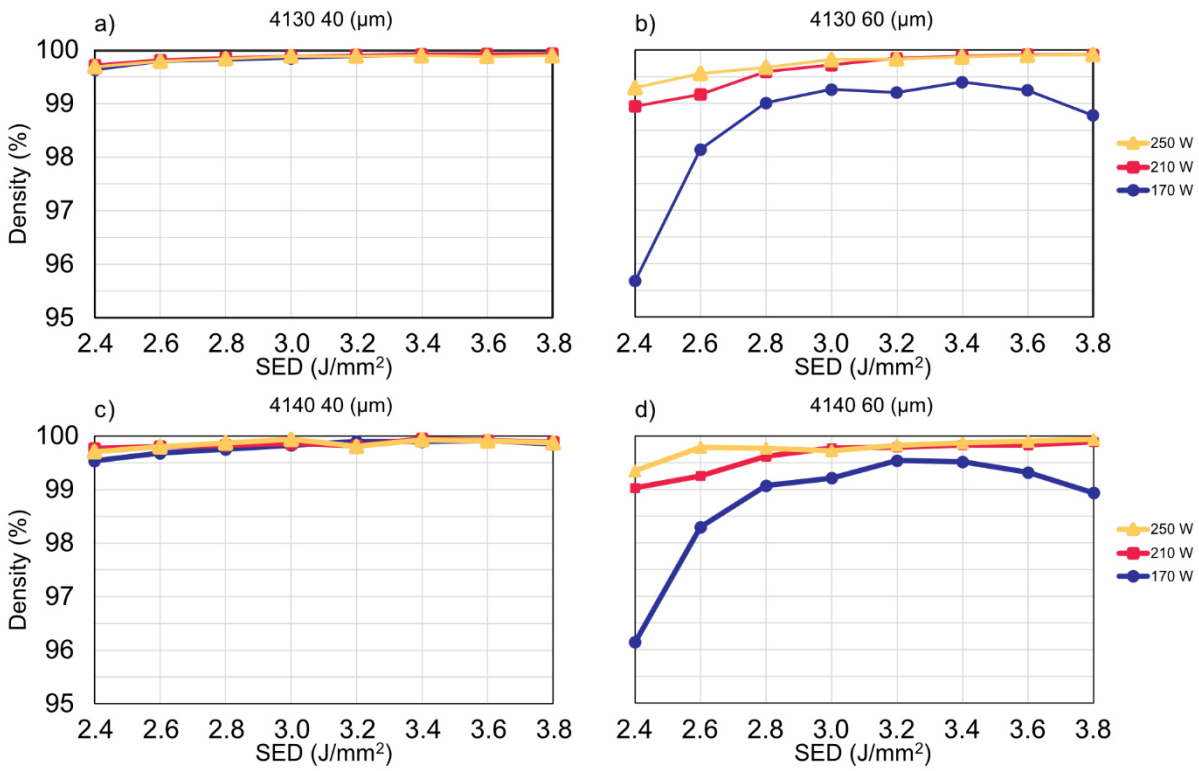

Figure 7. Influence of SED (J/mm^3) and laser power on density (%) a) - b) 4130 and c) - d) 4140 at 40 and 60 µm layer thickness

Influence of layer thickness on defects

The influence of layer thickness on density was further depicted by investigations of unetched micrographs at 2.4 J/mm^3 and 170 W, see Figure 8. From 20 to 60 µm layer thickness there is an increase in fraction of features characterised by sharp edges. In Figure 8 f), sharp features of up to 200 µm containing unmolten powder is seen which are typical traits of lack of fusion pores [58]. These pores are the main cause of lower density observed at 60 µm layer thickness and they are removed by enhancing the SED. The bar charts in Figure 9 reveals that increased SED promotes the formation of deeper melt pools which is suggested to ensure proper bonding between layers at larger layer thicknesses as the melt pool needs to melt more powder.

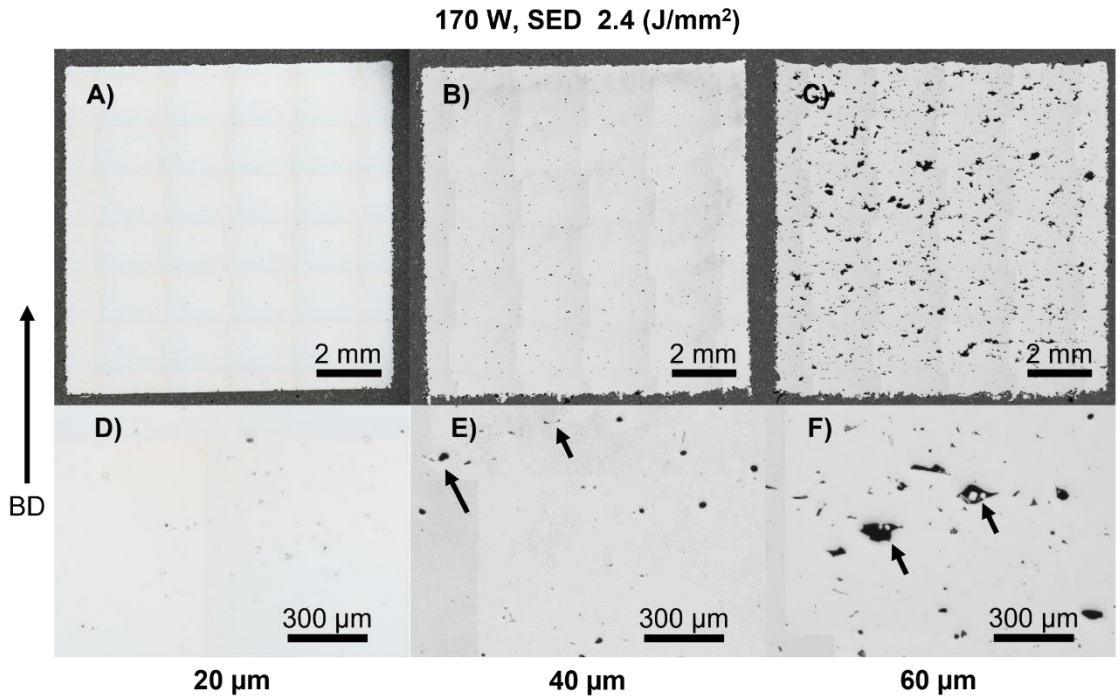

Figure 8. Pores present at low SED a) 20 µm layer thickness, b) 40 µm layer thickness and c) 60 µm layer thickness. Higher magnification d)- f) shows how the presence of sharp irregular pores, indicated by black arrows, increases in size with layer thickness. Trapped powder inside these pores indicates lack of fusion type porosity.

Influence of layer thickness on cold cracking

In some of the processed 4140 specimens, cracks were found located at the surface. These stretched from the surface inwards towards the bulk of the samples, perpendicular to the build direction (Figure 9c). Due to the small size, these cracks did not compromise the sample density. Previous work at 20 µm layer thickness could by microhardness and fractography connect the presence of these cracks to a cold cracking phenomenon [39]. The hardness and melt pool depths of each condition were evaluated to find a possible link between the process parameters and cracks. Figure 9a-b shows that the melt pool depth increases while the hardness decreases with increased SED. The hardness was slightly higher (~400 – 450 HV10) for the 4140 than for the 4130 alloy (~350 – 400 HV10) for SED of between 2.4 – 3.8 J/mm^2, with samples containing cracks being coloured red. Figure 9b shows that crack free samples are obtained at above 3.4 J/mm^2 for both layer thicknesses. This is likely attributed to the larger volume of material that is melted at larger SED that provides larger melt pools and increased in situ-tempering of the material [59]. Further, it is suggested that the higher carbon content increases the hardenability of the 4140 alloy compared to the 4130 alloy and the susceptibility to form cracks [39].

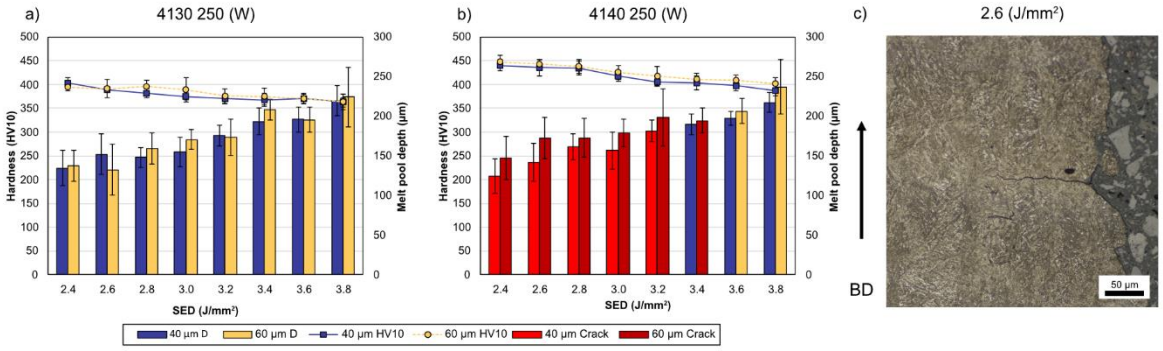

Figure 9. Hardness (HV10) and melt pool depth (µm) as a function of SED (J/mm^2) for a) 4130 and b) 4140 at 250 (W) laser power. Specimens containing cold cracks are coloured red.

Impact of build rate on cracking

Based on the findings of defects present within the investigated parameter range defined by SED in paper 1, the productivity performance was evaluated in terms of density and build rate for each alloy and layer thickness. Figure 10 depicts the compromise between density and build rate at the same range of scan speed (650 – 1500 mm/s) where the density values are separated by layer thickness and laser power. Both plots include a data point at 5.1 cm^3/h (yellow) from a reference study of the 4140 alloy at 20 µm layer thickness [33].

The largest build rates are found at 250 W laser power for both alloys as it was possible to provide densities above 99.8 % at larger scan speeds compared to the 170 W and 250 W processes. With respect to the reference point at 20 µm layer thickness the 4130 alloy reached 13.8 cm^3/h and 18.0 cm^3/h at increased layer thicknesses of 40 µm and 60 µm. This corresponded to increases in build rate by 170 % and 252 %, respectively. The lower build rates were reached for 4140 alloy due to cold cracks being present at larger scan speeds (11.0 cm^3/h and 15.0 cm^3/h) corresponding to increases in build rate by 115 % and 194 % compared to the reference study.

The main findings of paper 1 is that the carbon content limits the productivity of low alloy steels produced by PBF-LB. The build rate in this work was increased by increasing the scan speed which generated more shallow melt pools and less in situ – tempering that in combination with high residual stresses resulted in cold cracking. Thus, the build rates were larger in the 4130 alloy with lower carbon content.

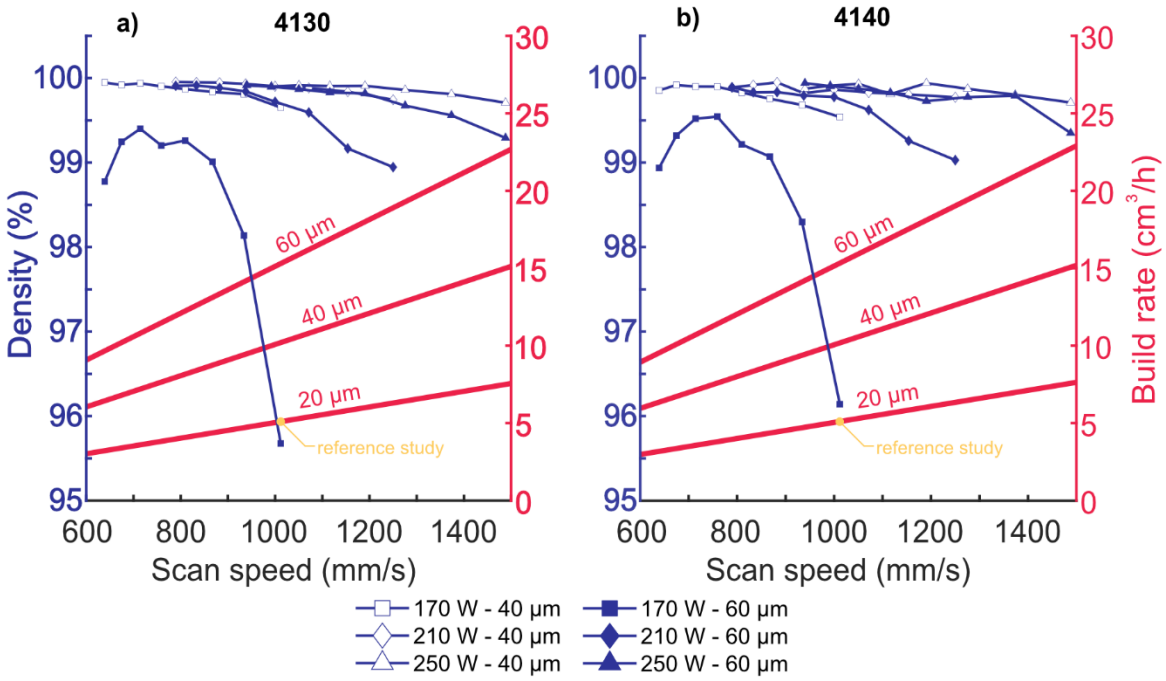

Figure 10. Density (%) as a function of scan speed (mm/s) and build rate (cm^3/h) for a) 4130 and b) 4140 produced samples. Solid lines of constant build rate (cm^3/h) are presented on the secondary y-axis and corresponds to the density measurements by layer thickness 40 µm and 60 µm. For each density measurement the build rate can be read from the solid lines for the corresponding layer thickness at that scan speed. The achieved build rate with the same machine and alloy in previous study [33] is plotted in yellow as a reference value at 20 µm layer thickness.

4.2 Summary of results Paper 2 – Pore characterization of 316L stainless steel

The productivity and build speed in paper 1 was evaluated by varying layer thickness and scan speed while the hatch distance was kept constant. To further understand the impact on main process parameters (also including hatch distance) on build rate, a wider parameter range was studied in paper 2. To isolate the impact of parameters on the porosity present at increased build rates the transition to a one phase material (316L) was made. It was hypothesized that by removing the martensitic phase transformation as a variable more direct conclusions could be gained concerning the relationship between build speed, microstructure and material properties.

VED vs Porosity

Figure 11 illustrates the feasibility of using the combined parameter VED and how well it correlates to obtained porosity when a wide range of parameters are varied. It is seen that

porosity decreases with increased VED on a global scale across the entire process region. However, differences of up to 7.5 % porosity were measured at the same VED. The highlighted micrographs show these differences to be attributed to the use of larger hatch distance rather than scan speed. Hence, the use of VED loses its usability when parameters are varied across a wide range. More consistent trends are found in paper 1 when hatch distance was kept constant.

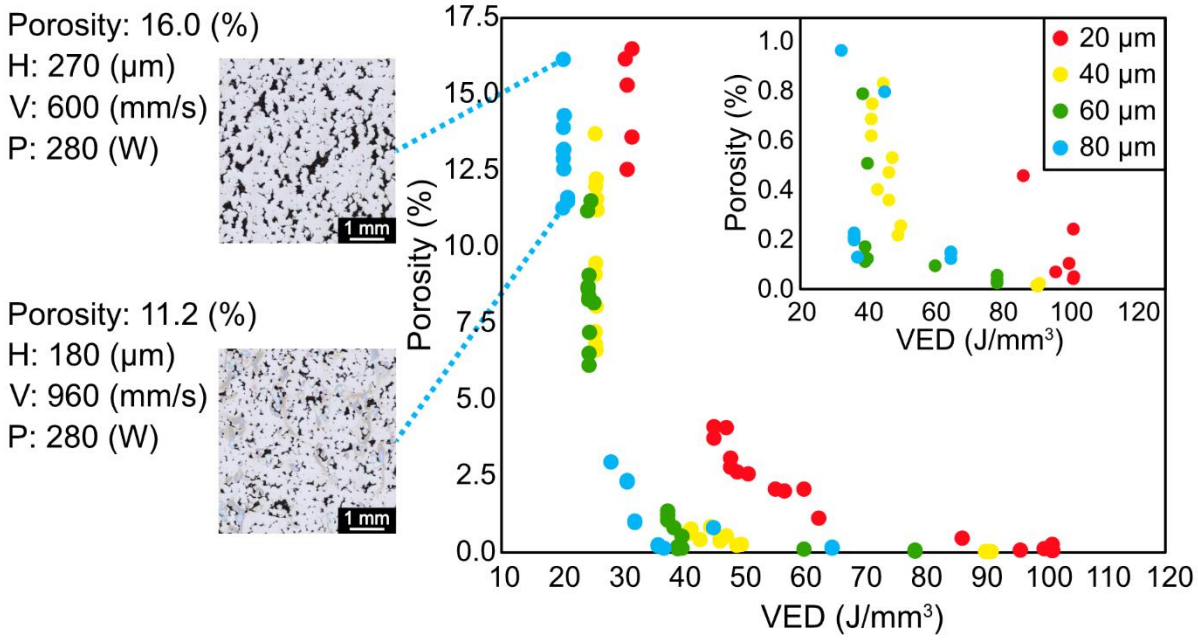

Figure 11. Influence of the combined process parameter VED J/mm^3 on porosity evolution at 20, 40, 60 and 80 µm layer thickness.

Regression model – influence of parameters on density

As the experiments in paper 2 did not show satisfactory trends between VED and porosity, predictive modelling was investigated as an option. According to equation (5), the density as a function of laser power, scan speed and hatch distance was predicted by performing linear regression at 20, 40, 60 and 80 µm layer thicknesses separately. The results of these regressions are summarised in Figure 12 as contour plots represented at a low 200 W and high 280 W laser power at each layer thickness. Each contour plot shows the interaction between hatch distance (x – axis), scan speed (y – axis) and the influence on density.

For a given layer thickness, the larger laser power (280 W) expands the regions of high density. This means that build speed can be increased by using larger hatch distance or scan

speeds while still obtaining desirable densification. Furthermore, the region of above 99.9 % density is reduced from 20 to 80 µm layer thickness. Figure 12b shows how this region is limited to the corner of low scan speed and low hatch distance. The four factor increase in layer thickness leads to a reduction of this region which is consistent with previous work [35] as this also means a reduction in the number of remelted layers by a factor of 4.

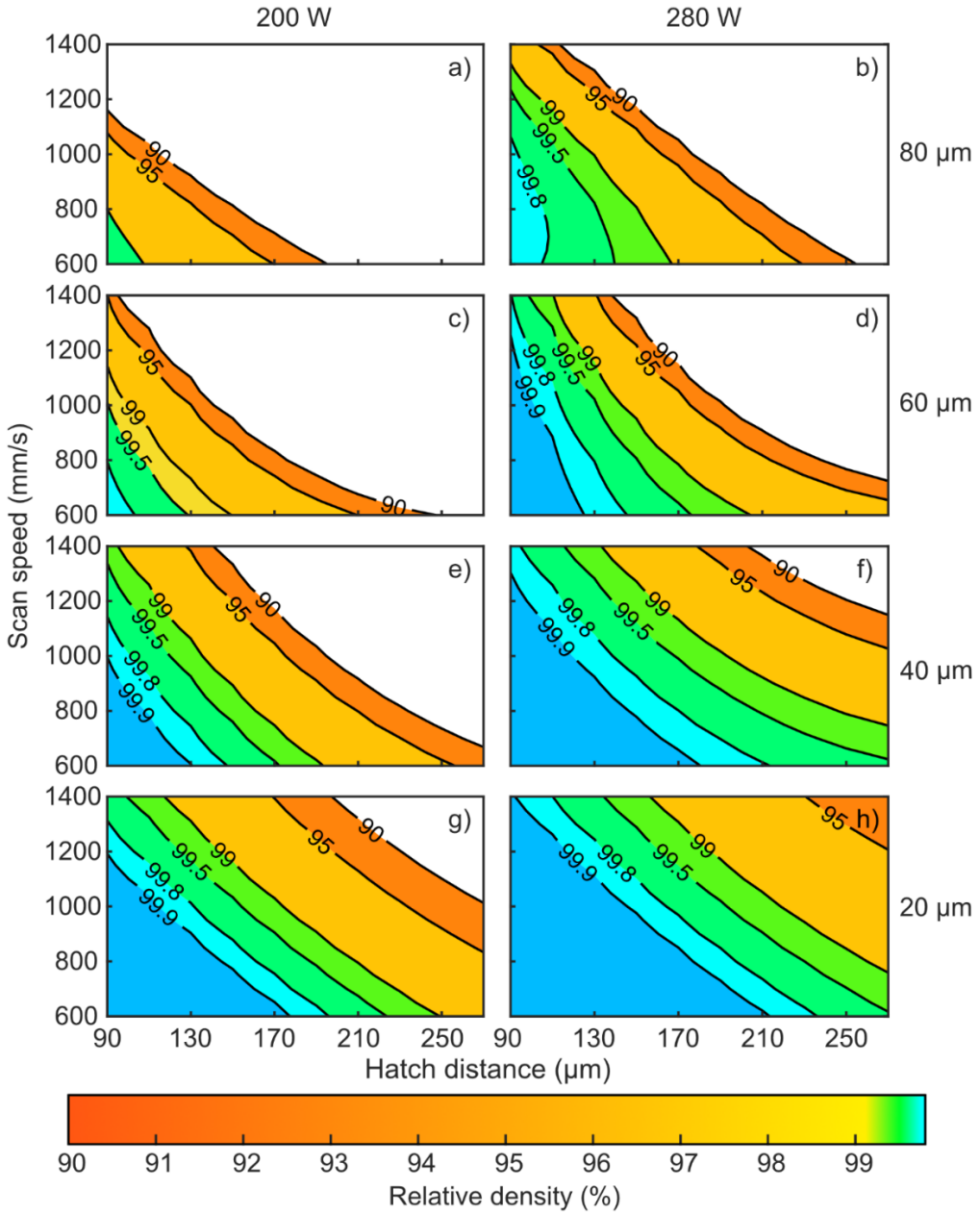

Figure 12. Contour surfaces illustrating the interaction between laser power, scan speed and hatch distance at 20, 40, 60 and 80 µm layer thickness separately.

Regression model vs actual density measurements and impact of build speed on pore characteristics

Figure 13 illustrates the predicted density as build rate increases in two dimensions by hatch distance (x-axis) and scan speed (y-axis), how the pore characteristics differ at increased build rates and how well predictions correspond to actual density measurements at 80 µm layer thickness. It is seen that the contour surface agrees well with the actual measurements, suggesting model accuracy. Similar figures at 20, 40 and 60 µm layer thickness can be found in the appendix of paper 2. The agreement between the predictions and actual density measurements indicates that regression modelling is more useful compared to the VED plots (Figure 11) for choosing appropriate parameters.

Starting from the reference sample in Figure 13c, that measured 99.9 % relative density and a build rate of 15.5 cm^3/h it is seen that build rate increases along either axis lowers the obtained density. At an 80 % increase in build rate of 28 cm^3/h (Figure b and Figure d) the density is larger by increasing scan speed 99.8 % as compared to 99.0 % density by increased hatch distance. Increase in build rate from the fully dense condition by ~120%, the two conditions in Figure 13a and Figure 13e are showing similar porosity content and build rate but different pore characteristics. In Figure 13a, there are larger individual pores with major axes aligned perpendicular to the build direction, whereas in Figure 13e the pores are of smaller size and are aligned parallel to the build direction. The orientation of pores is shown to have an impact on mechanical properties [37,60]. Therefore, detailed descriptions of these conditions are important.

Clear differences in pore characteristics between conditions of high build rates achieved by increasing hatch distance (Figure 13a) and scan speed (Figure 13e) was validated by image analysis. For pores larger than 100 µm, the average orientation angle was 70° in the case of increased hatch distance, meaning that they align close the build direction. In contrast, at increased scan speed, the orientation angle was 25°, indicating a pore orientation perpendicular to the build direction. Choo et al. [15] demonstrated that pores oriented perpendicular to the load direction exhibit inferior yield strength and ductility compared to parallelly oriented pores. Thus, the route of increasing the build rate affects the anisotropy of mechanical properties. Therefore, the choice of parameters for increasing the build rate should consider the load case in the final application.

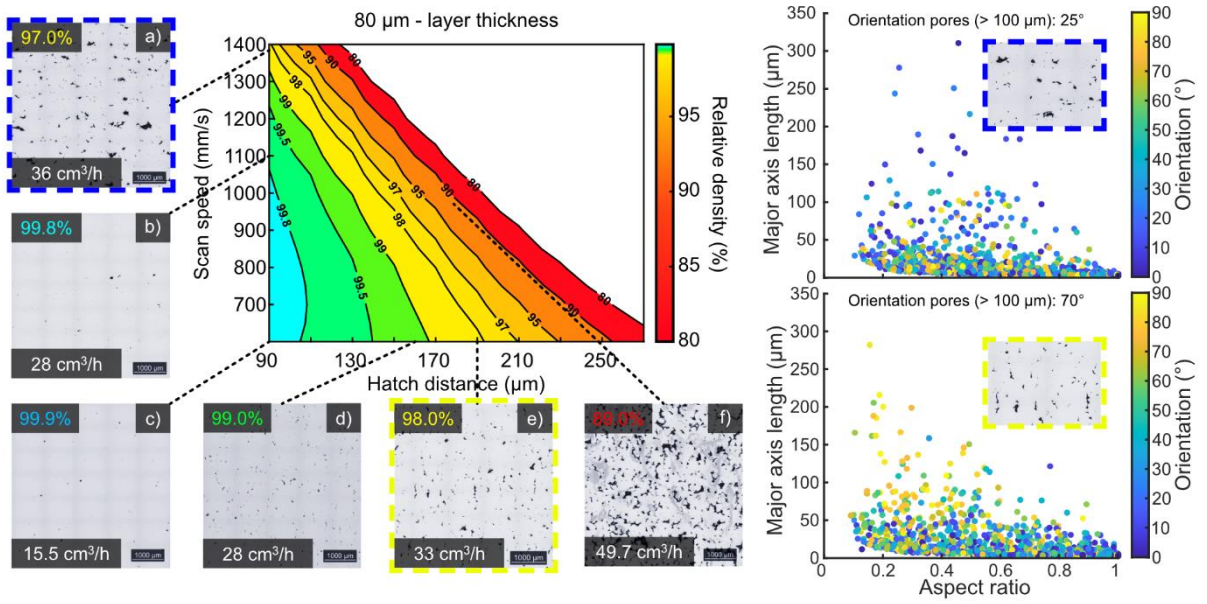

Figure 13. Influence of scan speed and hatch distance on relative density (%) at increased build rates and the impact on pore characteristics namely, size, aspect ratio and pore orientation.

Melt pool characteristics at large hatch distances

Paper 2 established good agreement between regression models and the actual density measurements and showed how similar build rates achieved by alternate processing routes (hatch distance or scan speed) had significantly different pore characteristics. To understand the development of these pores and to explain how larger hatch distance could be used at lower layer thickness while maintaining high densification, selected specimens were etched to reveal microstructural features namely the melt pools.

Studies of the last processed layer at 40 µm layer thickness revealed that melt pools could lack complete overlap between subsequent melt pools (Figure 14c and Figure 14d) but still lack the presence of pores at large hatch distances (230 µm and 250 µm). This is not the case at 80 µm layer thickness where triangular-shaped pores (Figure 14a) and complete lack of bonding (Figure 14) is seen at 160 µm and 190 µm. This corresponds to observations of the contour surfaces in Figure 8 where the use of lower layer thickness enables larger hatch distance. It is assumed that the remelting that occurs twice as often at 40 µm layer thickness can compensate for the lack of overlap in material that is deposited later compared to the 80 µm layer thickness (Figure 14a and Figure 14b).

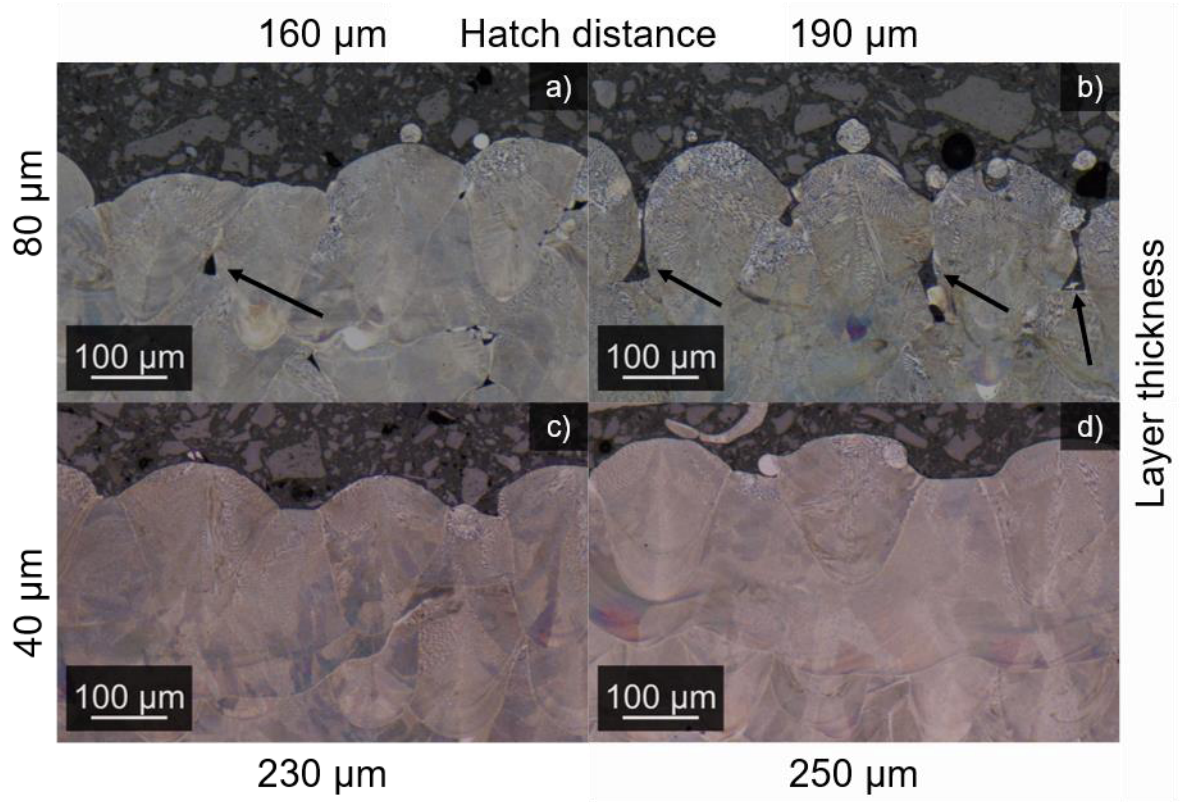

Figure 14. Melt pools of the final deposited layer revealed by etching at different layer thicknesses and hatch distances.

5. Conclusions

Based on the results provided in this thesis the following conclusion can be made:

What is the impact of PBF-LB process parameters on build speed during processing of iron-based alloys?

- The build rate can be improved by up to 252 % by increasing the layer thickness from 20 µm to 60 µm and still achieve high relative density (>99.8 %) for the 4130. The 4140 could be produced at a build rate increase by 194 %.
- Around 120% build rate increases in 316L achieved through either increased scan speed or hatch distance led to pores perpendicular or parallel to the build direction. The choice of parameter increase should therefore depend on the load direction of the printed component.
- When varying multiple process parameters (layer thickness, scan speed, hatch distance and laser power) in a wide range, up to 7.5% difference in porosity can be seen at the same VED value. This difference is mainly attributed to the wide range of hatch distance explored in paper 2.

What is the impact of increased build speed during PBF-LB processing on porosity characteristics and material properties?

- At high SED and 60 µm layer thickness for low alloy steels, lack of fusion was found at low laser power. These defects could be avoided by operating at a higher laser power. Thus, when increasing layer thickness, it is advised to use laser powers above 170 W.
- At low SED, sharp irregular pores were found that yielded relative densities below 99.8% at both layer thicknesses. However, the lack of fusion could be mitigated by increasing the SED which increases the melt pool depth and ensures proper bonding between subsequent layers.
- Cold cracking was found in AISI 4140 samples produced at 40 µm and 60 µm However, the cracks could be mitigated by increasing the SED >3.4 (J/mm^2), as it promotes the in-situ tempering during the PBF-LB process. This could be related to the decrease in sample hardness (~450 – 400 HV10) with increased SED.
- The use of large hatch distance in PBF-LB processing of 316L resulted in preferential orientation of elongated pores along the build direction when layer thickness is also large (80 µm). This phenomenon is not as prominent in samples built with 40 µm layer thickness. It is hypothesized that the use of smaller layer thickness incurs more remelting, which eliminates pores, or fills gaps between hatches.

6. Future work

Studies on the impact of increased build speeds on density and pore characteristics were performed by dedicated design of experiments and image analysis of the gained microstructures across a wide range of parameters. In this thesis, productivity increases by increasing main printing parameters was studied for two low alloy steels of different carbon contents and a 316L stainless steel. These studies established a general baseline for the impact of high build speed parameters on the porosity developed in the bulk material. However, several aspects still need further consideration to fully understand impact of increased build speed:

- Evaluation of how mechanical properties are affected by increased build speeds needs to be studied especially at conditions of similar build rate but different pore characteristics.
- X-ray computed tomography can provide better understanding concerning pore characteristics and their impact on mechanical properties.
- Increased build speed leads to rough surfaces which has not been considered at this point. Ways of enhancing surfaces will be studied both by developing contour parameters as well as post processing methods.
- The combination of high build rate printing parameters and hot isostatic pressing to further boost productivity.

Acknowledgements

I would like to thank my supervisor Professor Eduard Hryha and co-supervisor Dr. Zhuoer Chen for their guidance, support, and fruitful discussions during this part of my PhD journey.

Special thanks to my family and friends for your endless support during difficult times.

References

[1] D. Herzog, V. Seyda, E. Wycisk, C. Emmelmann, Additive manufacturing of metals, Acta Mater 117 (2016) 371–392. https://doi.org/10.1016/j.actamat.2016.07.019.

[2] T. DebRoy, H.L. Wei, J.S. Zuback, T. Mukherjee, J.W. Elmer, J.O. Milewski, A.M. Beese, A. Wilson-Heid, A. De, W. Zhang, Additive manufacturing of metallic components – Process, structure and properties, Prog Mater Sci 92 (2018) 112–224. https://doi.org/10.1016/j.pmatsci.2017.10.001.

[3] S. Sun, M. Brandt, M. Easton, Powder bed fusion processes, in: Laser Additive Manufacturing, Elsevier, 2017: pp. 55–77. https://doi.org/10.1016/B978-0-08-100433-3.00002-6.

[4] W. Zhang, W. Hou, L. Deike, C.B. Arnold, Using a Dual-laser System to Create Periodic Coalescence in Laser Powder Bed Fusion, Acta Mater 201 (2020) 14–22. https://doi.org/10.1016/j.actamat.2020.09.071.

[5] N. Haghdadi, M. Laleh, M. Moyle, S. Primig, Additive manufacturing of steels: a review of achievements and challenges, J Mater Sci 56 (2021) 64–107. https://doi.org/10.1007/s10853-020-05109-0.

[6] S. Sanchez, P. Smith, Z. Xu, G. Gaspard, C.J. Hyde, W.W. Wits, I.A. Ashcroft, H. Chen, A.T. Clare, Powder Bed Fusion of nickel-based superalloys: A review, Int J Mach Tools Manuf 165 (2021). https://doi.org/10.1016/j.ijmachtools.2021.103729.

[7] P.A. Rometsch, Y. Zhu, X. Wu, A. Huang, Review of high-strength aluminium alloys for additive manufacturing by laser powder bed fusion, Mater Des 219 (2022) 110779. https://doi.org/10.1016/j.matdes.2022.110779.

[8] T.S. Tshephe, S.O. Akinwamide, E. Olevsky, P.A. Olubambi, Additive manufacturing of titanium-based alloys- A review of methods, properties, challenges, and prospects, Heliyon 8 (2022) e09041. https://doi.org/10.1016/j.heliyon.2022.e09041.

[9] A. Vafadar, F. Guzzomi, A. Rassau, K. Hayward, Advances in metal additive manufacturing: A review of common processes, industrial applications, and current challenges, Applied Sciences (Switzerland) 11 (2021) 1–33. https://doi.org/10.3390/app11031213.

[10] C. Pauzon, E. Hryha, P. Forêt, L. Nyborg, Effect of argon and nitrogen atmospheres on the properties of stainless steel 316 L parts produced by laser-powder bed fusion, Mater Des 179 (2019). https://doi.org/10.1016/j.matdes.2019.107873.

[11] J.P. Oliveira, A.D. LaLonde, J. Ma, Processing parameters in laser powder bed fusion metal additive manufacturing, Mater Des 193 (2020) 1–12. https://doi.org/10.1016/j.matdes.2020.108762.

[12] M. Taghian, M. Hossein, E. Lannunziata, G. Del, L. Iuliano, A. Saboori, Laser powder bed fusion of metallic components : Latest progress in productivity , quality , and cost perspectives, Journal of Materials Research and Technology 27 (2023) 6484–6500. https://doi.org/10.1016/j.jmrt.2023.11.049.

[13] Z. Dong, Y. Liu, W. Wen, J. Ge, J. Liang, Effect of hatch spacing on melt pool and as-built quality during selective laser melting of stainless steel: Modeling and experimental approaches, Materials 12 (2018). https://doi.org/10.3390/ma12010050.

[14] M. Tang, P.C. Pistorius, J.L. Beuth, Prediction of lack-of-fusion porosity for powder bed fusion, Addit Manuf 14 (2017) 39–48. https://doi.org/10.1016/j.addma.2016.12.001.

[15] A. Leicht, M. Rashidi, U. Klement, E. Hryha, Effect of process parameters on the microstructure, tensile strength and productivity of 316L parts produced by laser powder bed fusion, Mater Charact 159 (2020) 110016. https://doi.org/10.1016/j.matchar.2019.110016.

[16] U. Scipioni Bertoli, A.J. Wolfer, M.J. Matthews, J.P.R. Delplanque, J.M. Schoenung, On the limitations of Volumetric Energy Density as a design parameter for Selective Laser Melting, Mater Des 113 (2017) 331–340. https://doi.org/10.1016/j.matdes.2016.10.037.

[17] A. Bobel, L.G. Hector, I. Chelladurai, A.K. Sachdev, T. Brown, W.A. Poling, R. Kubic, B. Gould, C. Zhao, N. Parab, A. Greco, T. Sun, In situ synchrotron X-ray imaging of 4140 steel laser powder bed fusion, Materialia (Oxf) 6 (2019) 100306. https://doi.org/10.1016/j.mtla.2019.100306.

[18] S.L. Campanelli, N. Contuzzi, P. Posa, A. Angelastro, Printability and microstructure of selective laser melting of WC/Co/Cr powder, Materials 12 (2019). https://doi.org/10.3390/ma12152397.

[19] A. Gatto, M.L. Gatto, R. Groppo, D. Munteanu, P. Mengucci, Influence of laser powder bed fusion process parameters on the properties of CuZn42 components: case study of the laser surface energy density, Progress in Additive Manufacturing 8 (2023) 843–855. https://doi.org/10.1007/s40964-022-00361-z.

[20] I. Yadroitsev, A. Gusarov, I. Yadroitsava, I. Smurov, Single track formation in selective laser melting of metal powders, J Mater Process Technol 210 (2010) 1624–1631. https://doi.org/10.1016/j.jmatprotec.2010.05.010.

[21] L. Guo, H. Wang, H. Liu, Y. Huang, Q. Wei, C.L.A. Leung, Y. Wu, H. Wang, Understanding keyhole induced-porosities in laser powder bed fusion of aluminum and elimination strategy, Int J Mach Tools Manuf 184 (2023). https://doi.org/10.1016/j.ijmachtools.2022.103977.

[22] A. Sola, A. Nouri, Microstructural porosity in additive manufacturing: The formation and detection of pores in metal parts fabricated by powder bed fusion, J Adv Manuf Process 1 (2019) 1–21. https://doi.org/10.1002/amp2.10021.

[23] N. Yodoshi, T. Endo, N. Masahashi, Evaluation of porosity in gas-atomized powder by synchrotron X-ray CT and investigation of the effect of gas species, Mater Trans 62 (2021) 1549–1555. https://doi.org/10.2320/matertrans.MT-Y2021001.

[24] C. Du, Y. Zhao, J. Jiang, Q. Wang, H. Wang, N. Li, J. Sun, Pore defects in Laser Powder Bed Fusion: Formation mechanism, control method, and perspectives, J Alloys Compd 944 (2023) 169215. https://doi.org/10.1016/j.jallcom.2023.169215.

[25] W.H. Kan, L.N.S. Chiu, C.V.S. Lim, Y. Zhu, Y. Tian, D. Jiang, A. Huang, A critical review on the effects of process-induced porosity on the mechanical properties of alloys fabricated by laser powder bed fusion, J Mater Sci 57 (2022) 9818–9865. https://doi.org/10.1007/s10853-022-06990-7.

[26] T. Montalbano, B.N. Briggs, J.L. Waterman, S. Nimer, C. Peitsch, J. Sopcisak, D. Trigg, S. Storck, Uncovering the coupled impact of defect morphology and microstructure on the tensile behavior of Ti-6Al-4V fabricated via laser powder bed fusion, J Mater Process Technol 294 (2021) 117113. https://doi.org/10.1016/j.jmatprotec.2021.117113.

[27] Z. Li, H. Li, J. Yin, Y. Li, Z. Nie, X. Li, D. You, K. Guan, W. Duan, L. Cao, D. Wang, L. Ke, Y. Liu, P. Zhao, L. Wang, K. Zhu, Z. Zhang, L. Gao, L. Hao, A Review of Spatter in

Laser Powder Bed Fusion Additive Manufacturing: In Situ Detection, Generation, Effects, and Countermeasures, Micromachines (Basel) 13 (2022). https://doi.org/10.3390/mi13081366.

[28] Z.A. Young, Q. Guo, N.D. Parab, C. Zhao, M. Qu, L.I. Escano, K. Fezzaa, W. Everhart, T. Sun, L. Chen, Types of spatter and their features and formation mechanisms in laser powder bed fusion additive manufacturing process, Addit Manuf 36 (2020) 101438. https://doi.org/10.1016/j.addma.2020.101438.

[29] P.A. Hooper, Melt pool temperature and cooling rates in laser powder bed fusion, Addit Manuf 22 (2018) 548–559. https://doi.org/10.1016/j.addma.2018.05.032.

[30] J. Platl, H. Leitner, C. Turk, A.G. Demir, B. Previtali, R. Schnitzer, Defects in a Laser Powder Bed Fused Tool Steel, Adv Eng Mater 23 (2021) 1–11. https://doi.org/10.1002/adem.202000833.

[31] W. Wang, S. Kelly, A Metallurgical Evaluation of the Powder-Bed Laser Additive Manufactured 4140 Steel Material, Jom 68 (2016) 869–875. https://doi.org/10.1007/s11837-015-1804-y.

[32] W. Hearn, E. Hryha, Effect of Carbon Content on the Processability of Fe-C Alloys Produced by Laser Based Powder Bed Fusion, Front Mater 8 (2022) 1–10. https://doi.org/10.3389/fmats.2021.800021.

[33] W. Hearn, P. Harlin, E. Hryha, Development of powder bed fusion–laser beam process for AISI 4140, 4340 and 8620 low-alloy steel, Powder Metallurgy 66 (2023) 94–106. https://doi.org/10.1080/00325899.2022.2134083.

[34] H. Fayazfar, M. Salarian, A. Rogalsky, D. Sarker, P. Russo, V. Paserin, E. Toyserkani, A critical review of powder-based additive manufacturing of ferrous alloys: Process parameters, microstructure and mechanical properties, Mater Des 144 (2018) 98–128. https://doi.org/10.1016/j.matdes.2018.02.018.

[35] A. Leicht, M. Fischer, U. Klement, L. Nyborg, E. Hryha, Increasing the Productivity of Laser Powder Bed Fusion for Stainless Steel 316L through Increased Layer Thickness, J Mater Eng Perform 30 (2021) 575–584. https://doi.org/10.1007/s11665-020-05334-3.

[36] D. Riabov, A. Leicht, J. Ahlström, E. Hryha, Investigation of the strengthening mechanism in 316L stainless steel produced with laser powder bed fusion, Materials Science and Engineering A 822 (2021). https://doi.org/10.1016/j.msea.2021.141699.

[37] T. Ronneberg, C.M. Davies, P.A. Hooper, Revealing relationships between porosity, microstructure and mechanical properties of laser powder bed fusion 316L stainless steel through heat treatment, Mater Des 189 (2020) 108481. https://doi.org/10.1016/j.matdes.2020.108481.

[38] X. Li, Y.H. Tan, H.J. Willy, P. Wang, W. Lu, M. Cagirici, C.Y.A. Ong, T.S. Herng, J. Wei, J. Ding, Heterogeneously tempered martensitic high strength steel by selective laser melting and its micro-lattice: Processing, microstructure, superior performance and mechanisms, Mater Des 178 (2019) 107881. https://doi.org/10.1016/j.matdes.2019.107881.

[39] W. Hearn, R. Steinlechner, E. Hryha, Laser-based powder bed fusion of non-weldable low-alloy steels, Powder Metallurgy 0 (2021) 1–12. https://doi.org/10.1080/00325899.2021.1959695.

[40] T. Fedina, J. Sundqvist, A.F.H. Kaplan, Spattering and oxidation phenomena during recycling of low alloy steel powder in Laser Powder Bed Fusion, Mater Today Commun 27 (2021) 102241. https://doi.org/10.1016/j.mtcomm.2021.102241.

[41] M. Abdelwahed, S. Bengtsson, R. Casati, A. Larsson, S. Petrella, M. Vedani, Effect of water atomization on properties of type 4130 steel processed by L-PBF, Mater Des 210 (2021) 110085. https://doi.org/10.1016/j.matdes.2021.110085.

[42] M. Abdelwahed, R. Casati, A. Larsson, S. Petrella, S. Bengtsson, M. Vedani, On the Recycling of Water Atomized Powder and the Effects on Properties of L-PBF Processed 4130 Low-Alloy Steel, Materials 15 (2022). https://doi.org/10.3390/ma15010336.

[43] J. Damon, R. Koch, D. Kaiser, G. Graf, S. Dietrich, V. Schulze, Process development and impact of intrinsic heat treatment on the mechanical performance of selective laser melted AISI 4140, Addit Manuf 28 (2019) 275–284. https://doi.org/10.1016/j.addma.2019.05.012.

[44] E. Jelis, M.R. Hespos, N.M. Ravindra, Process Evaluation of AISI 4340 Steel Manufactured by Laser Powder Bed Fusion, J Mater Eng Perform 27 (2018) 63–71. https://doi.org/10.1007/s11665-017-2989-8.

[45] E. Jelis, M. Hespos, S.L. Groeschler, R. Carpenter, L-PBF of 4340 Low Alloy Steel: Influence of Feedstock Powder, Layer Thickness, and Machine Maintenance, J Mater Eng Perform 28 (2019) 693–700. https://doi.org/10.1007/s11665-018-3739-2.

[46] K. Li, T. Yang, N. Gong, J. Wu, X. Wu, D.Z. Zhang, L.E. Murr, Additive manufacturing of ultra-high strength steels: A review, J Alloys Compd 965 (2023) 171390. https://doi.org/10.1016/j.jallcom.2023.171390.

[47] C. Aumayr, J. Platl, H. Zunko, C. Turk, Additive Manufacturing of a Low-alloyed Engineering Steel Additive Fertigung eines niedriglegierten Einsatzstahls, BHM Berg- Und Hüttenmännische Monatshefte 165 (2020) 137–142. https://doi.org/10.1007/s00501-020-00966-3.

[48] O. Diegel, A. Nordin, D. Motte, A Practical Guide to Design for Additive Manufacturing, 2019.

[49] C.S. Frandsen, M.M. Nielsen, A. Chaudhuri, J. Jayaram, K. Govindan, In search for classification and selection of spare parts suitable for additive manufacturing: a literature review, Int J Prod Res 58 (2020) 970–996. https://doi.org/10.1080/00207543.2019.1605226.

[50] C. Schwerz, F. Schulz, E. Natesan, L. Nyborg, Increasing productivity of laser powder bed fusion manufactured Hastelloy X through modification of process parameters, J Manuf Process 78 (2022) 231–241. https://doi.org/10.1016/J.JMAPRO.2022.04.013.

[51] S. Wang, Y. Liu, W. Shi, B. Qi, J. Yang, F. Zhang, D. Han, Y. Ma, Research on high layer thickness fabricated of 316L by selective laser melting, Materials 10 (2017). https://doi.org/10.3390/ma10091055.

[52] EOS GmbH – Electro Optical Systems, “EOS 316L Stainless Steel AM Material Data Sheet”, [Online]. Available: https://www.eos.info/05-datasheet-images/Assets_MDS_Metal/EOS_StainlessSteel_316l/material_datasheet_eos_stainlesssteel_316l_en_web.pdf.

[53] W. Hearn, Development of Structural Steels for Powder Bed Fusion – Laser Beam, 2023. https://research.chalmers.se/publication/534092%0Ahttps://research.chalmers.se/publication/534092/file/534092_Fulltext.pdf.

[54] C.A. Schneider, W.S. Rasband, K.W. Eliceiri, NIH Image to ImageJ: 25 years of image analysis, Nat Methods 9 (2012) 671–675. https://doi.org/10.1038/nmeth.2089.

[55] A. Ceramics, A. Ceramics, K. Hard-, A.B. Hardness, V. Hardness, S. Hardness, K. Hardness, L. Hardness, C. Techniques, P. Control, C. Laboratories, Standard Test Method for Microindentation Hardness of Materials BT - Standard Test Method for Microindentation Hardness of Materials, (17AD) 1–40. https://doi.org/10.1520/E0384-17.

[56] J. Damon, R. Koch, D. Kaiser, G. Graf, S. Dietrich, V. Schulze, Process development and impact of intrinsic heat treatment on the mechanical performance of selective laser melted AISI 4140, Addit Manuf 28 (2019) 275–284. https://doi.org/10.1016/j.addma.2019.05.012.

[57] P. Paradise, D. Patil, N. Van Handel, S. Temes, A. Saxena, D. Bruce, Improving Productivity in the Laser Powder Bed Fusion of Inconel 718 by Increasing Layer Thickness : Effects on Mechanical Behavior, J Mater Eng Perform in press (2022). https://doi.org/10.1007/s11665-022-06961-8.

[58] R. Snell, S. Tammas-Williams, L. Chechik, A. Lyle, E. Hernández-Nava, C. Boig, G. Panoutsos, I. Todd, Methods for Rapid Pore Classification in Metal Additive Manufacturing, Jom 72 (2020) 101–109. https://doi.org/10.1007/s11837-019-03761-9.

[59] W. Hearn, K. Lindgren, J. Persson, E. Hryha, In situ tempering of martensite during laser powder bed fusion of Fe-0.45C steel, Materialia (Oxf) 23 (2022). https://doi.org/10.1016/j.mtla.2022.101459.

[60] H. Choo, L.P. White, X. Xiao, C.C. Sluss, D. Morin, E. Garlea, Deformation and fracture behavior of a laser powder bed fusion processed stainless steel: In situ synchrotron x-ray computed microtomography study, Addit Manuf 40 (2021) 101914. https://doi.org/10.1016/j.addma.2021.101914.